JOURNAL OF SYNCHROTRON RADIATION
ISSN 1600-5775

Received 24 November 2016
Accepted 9 July 2017

Edited by G. E. Ice, Oak Ridge National Laboratory, USA

Keywords: confocal XAS; mobile endstation; sacrificial red glaze; depth-dependent valence distribution.

Confocal depth-resolved fluorescence micro-X-ray absorption spectroscopy for the study of cultural heritage materials: a new mobile endstation at the Beijing Synchrotron Radiation Facility

Guang Chen,[a,b] Shengqi Chu,[b] Tianxi Sun,[c] Xuepeng Sun,[c] Lirong Zheng,[b] Pengfei An,[b] Jian Zhu,[d] Shurong Wu,[e] Yonghua Du[f]* and Jing Zhang[b]*

[a]Institute of Health Sciences, Anhui University, Hefei 230601, People's Republic of China, [b]Beijing Synchrotron Radiation Facility, Institute of High Energy Physics, Chinese Academy of Sciences, Beijing 100049, People's Republic of China, [c]College of Nuclear Science and Technology, Beijing Normal University, Beijing 100975, People's Republic of China, [d]Department of Scientific History and Archaeometry, University of Chinese Academy of Sciences, Beijing 100949, People's Republic of China, [e]Jingdezhen Ceramics Institute of Archaeology, Jingdezhen 333001, People's Republic of China, and [f]Heterogeneous Catalysis, Institute of Chemical and Engineering Sciences, Agency for Science, Technology and Research, 1 Pesek Road, Jurong Island 627833, Singapore.
*Correspondence e-mail: du_yonghua@ices.a-star.edu.sg, jzhang@ihep.ac.cn

A confocal fluorescence endstation for depth-resolved micro-X-ray absorption spectroscopy is described. A polycapillary half-lens defines the incident beam path and a second polycapillary half-lens at 90° defines the probe sample volume. An automatic alignment program based on an evolutionary algorithm is employed to make the alignment procedure efficient. This depth-resolved system was examined on a general X-ray absorption spectroscopy (XAS) beamline at the Beijing Synchrotron Radiation Facility. Sacrificial red glaze (AD 1368–1644) china was studied to show the capability of the instrument. As a mobile endstation to be applied on multiple beamlines, the confocal system can improve the function and flexibility of general XAS beamlines, and extend their capabilities to a wider user community.

1. Introduction

X-ray absorption spectroscopy (XAS) is a powerful method for determining the local chemistry and structure of materials (Gautier-Soyer, 1998; Aksenov *et al.*, 2006; Rehr & Ankudinov, 2005). Standard XAS experiments are typically performed on homogeneous samples with millimeter-sized X-ray beams in transmission or fluorescence detection mode. However, in cultural heritage studies, objects are typically precious, heterogeneous and complex. Spatially resolved spectroscopic information is required to map chemical speciation, and also to provide insight into their artifact fabrication, alteration, restoration and preservation. This information helps to better understand the objects' past and can be used to predict the material's evolution, which is essential for preservation efforts.

In the last few years several attempts have been made to improve spatially resolved XAS measurements. Confocal micro-XAS is of increasing interest (Kanngießer *et al.*, 2011). In confocal mode, a probing volume is created by the foci of two optics; the first one placed in an excitation channel and the second one in a detection channel (Kanngießer *et al.*, 2003; Janssens *et al.*, 2004; Malzer & Kanngießer, 2005; Sun & Ding, 2015). Confocal detection restricts the probed fraction of the sample to an ellipsoidal volume allowing depth-resolved XAS

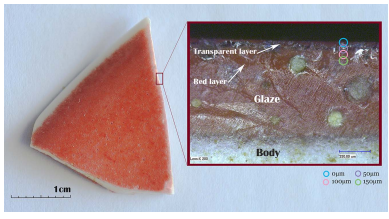

© 2017 International Union of Crystallography

(Denecke *et al.*, 2009; Zoeger *et al.*, 2008; Nakano *et al.*, 2011). Polycapillary confocal XAS has been established at the DUBBLE XAS station of the European Synchrotron Radiation Facility (BM26A) and the micro beamline of Berlin's synchrotron radiation facility BESSY II (Silversmit *et al.*, 2010). With the help of the confocal XAS method, Tack *et al.* (2016) reported depth-resolved micro-XAS studies of chemically strengthened boroaluminosilicate glasses; Lühl *et al.* (2014) exploited the manufacturing process of the Attic Black Glaze; Silversmit *et al.* (2009) also presented confocal XANES (X-ray absorption near-edge structure) data for a three-dimensional-resolved Fe *K*-XANES study on mineral inclusions within rare natural diamonds. Zi *et al.* (2015) combined a polycapillary half-lens (PHL) and Kirkpatrick–Baez mirrors to establish confocal XANES at beamline BL15U of the Shanghai Synchrotron Radiation Facility (SSRF), and applied this method to study the stratified structure of different paints in the Forbidden City. More recently, Choudhury *et al.* (2015) applied a spoked channel array to confocal XAS of medieval stained glass, which was carried out at the 20ID-B (PNC/XSD) beamline of the Advanced Photon Source at Argonne National Laboratory. These demonstrations opened up the way for unprecedented non-destructive investigations of cultural heritage materials (Kanngießer *et al.*, 2003; Wei *et al.*, 2008; Nakano & Tsuji, 2009; Guilherme *et al.*, 2011).

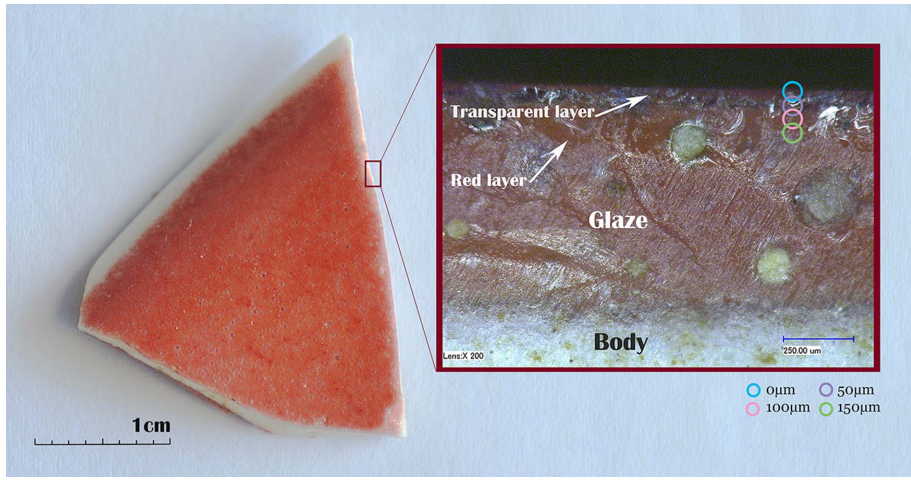

Figure 1
A piece of sacrificial red glaze and its micro-section photograph taken from the side. The circles illustrate the XANES scan range in the depth direction.

Despite these recent advances, it remains a great challenge to set up confocal micro-XAS in terms of sample speciation, beamline characteristics and efficient alignment procedure. Beijing Synchrotron Radiation Facility (BSRF) is a first-generation parasitic light source of the Beijing Electron and Positron Collider. The 1W1B and 1W2B XAS stations at BSRF are general-purpose instruments. To support the significant requirement of cultural heritage protection, a confocal depth-resolved micro-XAS setup has been implemented at an XAS station. Since the general mode and confocal detector mode co-exist in the operation of the XAS station, the confocal devices are assembled and disassembled frequently for the various users. However, conventional optimization of the confocal configuration is carried out *via* manual intervention, which is severely time-consuming. Here, with appropriate pre-focusing by a toroidal mirror, the first PHL is used as an effective re-focusing device for producing microbeams with high flux density and large angular divergence, and the second PHL is used in a detection channel. An automatic alignment program based on an evolutionary algorithm (Xi *et al.*, 2017) was introduced in the confocal system, which can greatly reduce the alignment time from several hours to less than 30 min. The feasibility of this approach is illustrated with a depth-resolved XAS analysis of sacrificial red glaze (AD 1368–1644) from China, which can act as the basis for a large-scale analysis of a wide range of ancient decorated specimens.

2. Experiment

2.1. Sample

A piece of sacrificial red glaze (shown in Fig. 1) from the Jingdezhen imperial kiln from the Xuande period of the Ming dynasty (AD 1398–1435), named XD1, was supplied by the Jingdezhen Ceramic Archaeological Institute. The Jingdezhen Ceramic Archaeological Institute excavated the imperial kiln site in 2010 and discovered precious specimens of this type in strata from the early Ming dynasty. The sample belongs to the initial stage of a sacrificial red glaze product in China and represents the royal aesthetic and the highest quality of ancient Chinese ceramics. Fig. 1 also shows a micro-section photograph of XD1, showing a transparent layer and a red layer.

2.2. Instrumentation

The experiments were performed at the 1W2B beamline of BSRF. The electron energy of the storage ring was 2.5 GeV and the beam current 150–250 mA. The horizontal and vertical angular acceptances of the source are 0.389 mrad and 0.15 mrad, respectively. The optical layout mainly consists of a collimating mirror, fixed-exit Si(111) double-crystal monochromator and toroidal mirror. The 1W2B beamline covers the energy range 5–18 keV, providing a focus of 1.0 mm (H) × 0.6 mm (V) full width at half-maximum (FWHM) with a photon flux of 3×10^{11} photons s^{-1} at 9 keV.

As shown in Fig. 2, re-focusing was achieved using a large-acceptance PHL (entrance diameter 5.6 mm, optic length 40 mm, exit diameter 4.3 mm and focal distance 14 mm) manufactured by the Beijing Normal University of China. The holder of the PHL was mounted on an xyz' positioner, with translational, rotary and tilt stages that provide the necessary

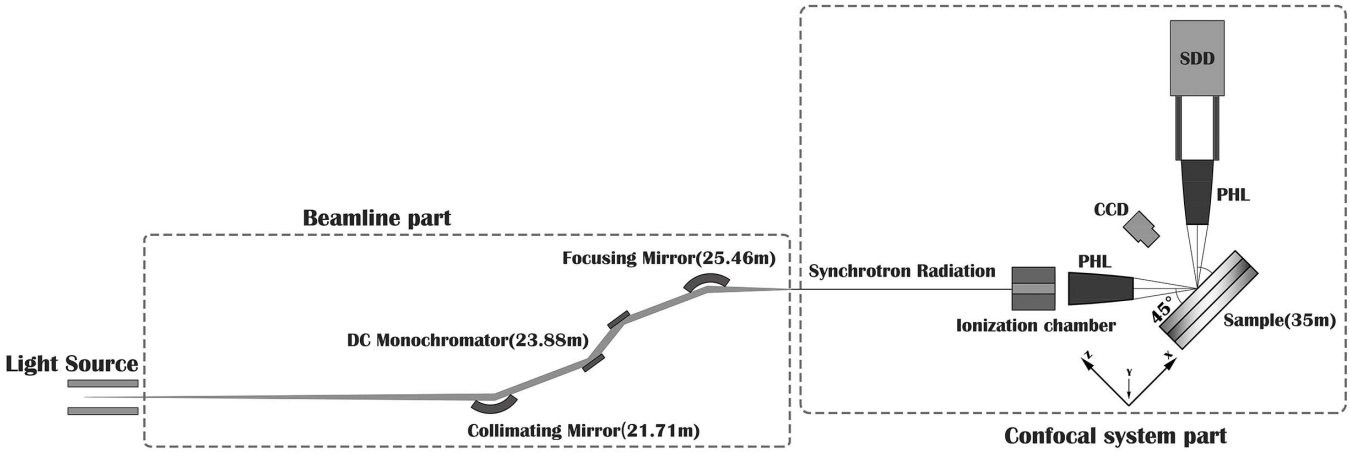

Figure 2
Scheme of the confocal depth-resolved micro-XAS setup at 1W2B, Beijing Synchrotron Radiation Facility.

degrees of freedom for the PHL alignment. The first ionization chamber, located in front of the sample, and the first PHL to monitor the incident X-ray beam intensity were used to normalize the fluorescence intensity. Behind the sample, a second ionization chamber is placed to record the transmitted beam intensity. A spot size of 53 µm FWHM was measured for the focused beam with a photon flux of 0.9×10^{11} photons s^{-1} at 9 keV. A second glass PHL, also from the Beijing Normal University of China (entrance diameter 5.5 mm, optical length 20.6 mm, output diameter 2.6 mm, focal distance 18 mm and focal spot 57 µm at 9 keV), was mounted in front of the energy-dispersive detector rigidly to achieve the confocal detection geometry. An Amptek silicon drift detector (Si SDD) was used to detect the fluorescence radiation. The energy resolution of this detector was 125 eV at 5.9 keV, and its maximum count rate was 5.0×10^5 s^{-1}. The sample was placed on a goniometer head fixed to an *XYZ* and rotation stage. A photograph of the confocal set-up at BSRF is given in Fig. 3.

In order to obtain the probing volume in terms of depth, a 7.5 µm-thick Ni foil was scanned through the X-ray beam. By means of the SDD the fluorescent X-ray intensity of the Ni *Kα* line was recorded during a live time of 3 s per translation step. By plotting the intensity as a function of the translation distance, Gaussian-like profiles were obtained, as shown in Fig. 4. The probing volume size FWHM, $\mathrm{FWHM_{confocalvolume}}$, is related to the foil thickness d and the FWHM of fluorescent intensity $\mathrm{FWHM_{intensity}}$ according to (Janssens *et al.*, 2004)

$$\mathrm{FWHM^2_{intensity}} = \mathrm{FWHM^2_{confocalvolume}} + d^2.$$

The probing volume size at 9 keV is 72 µm in the depth direction. The resulting ellipsoidal detection volume is 72 µm × 53 µm × 57 µm at the Cu *K*-edge. Taking into account the photon flux of the first-generation parasitic light source the probing volume is actually an advantage when performing studies, especially for archaeological stratified-like samples.

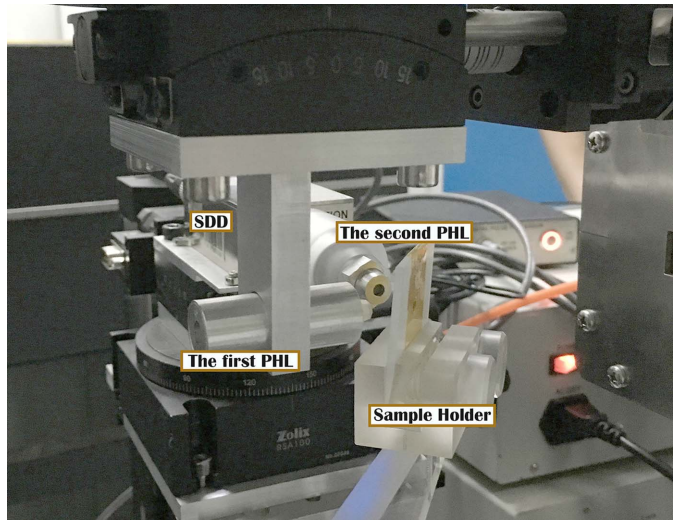

Figure 3
Photograph of the confocal setup at Beijing Synchrotron Radiation Facility.

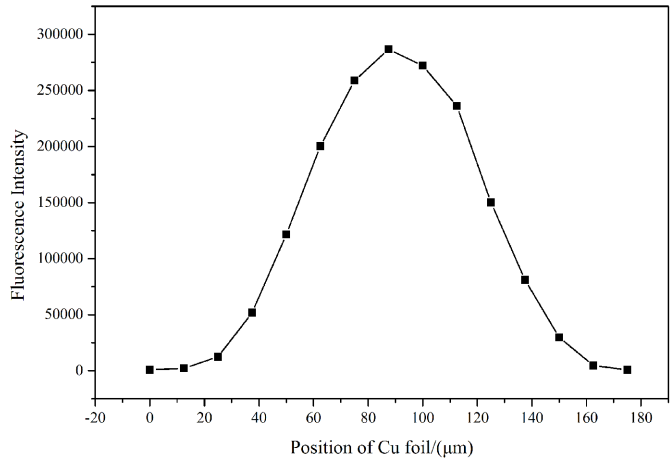

Figure 4
Fluorescence intensity *versus* translation distance of a Ni (7.5 µm) foil through the confocal micro-volume at 9 keV.

2.3. Alignment procedure

The first PHL was adjusted to obtain the highest transmitted beam intensity. One-percent $CuSO_4$ was used as a liquid secondary target (Peng *et al.*, 2013) at the sample position. The second PHL was roughly placed in the confocal configuration with the first PHL and the target. After pre-alignment, a program based on an evolutionary algorithm was applied in order to search for the optimal confocal arrangement. A flow chart showing the alignment system is outlined in Fig. 5. The *XYZ* position of the stepper motors (SMs) is used to monitor the conditions of the second PHL. The aim of the optimization is to reach the maximum intensity accepted by the SDD as the best alignment of the PHL through the evolution of the position of the SMs, which is automatically controlled by the evolutionary algorithm modules of the *AI-BL*1.0 program.

For the test performed in the second PHL, the initial SM position was fixed on the pre-alignment. Each SM was moved between −1.5 mm and +1.5 mm; namely, the focal spot of the PHL was adjusted within a 3 mm × 3 mm × 3 mm area space. The fluorescence of the Cu *Kα* line was collected using the SDD. Initially the fluorescence intensity was very weak at the sample position due to a misalignment of the lens. During the adjustment, 50 generations (a parameter in *AI-BL* which is a termination criterion in the evolutionary algorithm) was set. The PHL condition was optimized to maximize the fluorescence intensity of the Cu *Kα* line at the sample position monitored by the SDD. The system was typically able to find the optimal solution within 38 generations, which took 1543 s, as shown in Fig. 6, demonstrating that this method can optimize the optical components efficiently.

2.4. XAS data and analysis

Depth profiles were obtained by moving the sample stepwise into the probing volume and monitoring the Cu fluorescence intensity (with an excitation energy of 9 keV). A XANES scan of the first point (0 µm) was determined to be at the position of the maximum point of the profile. Depth-resolved XANES scans were acquired in 50 µm steps. The

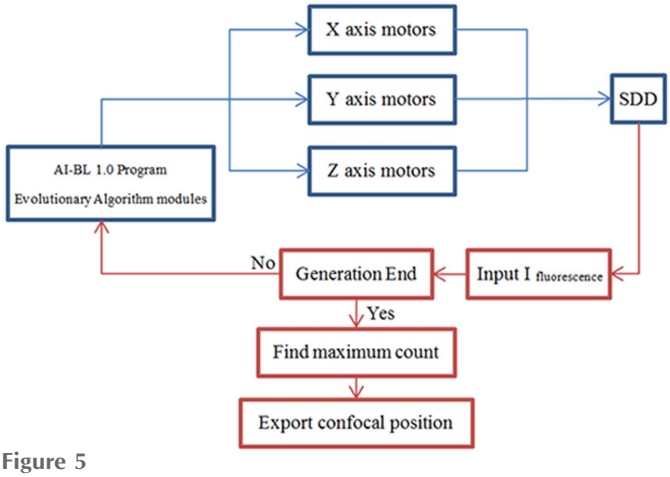

Figure 5
Flow chart showing the alignment system.

Table 1
XANES scanning parameters.

Start energy (eV)	End energy (eV)	Energy step (eV)	Time per point (s)
−120	−20	5	5
−20	50	0.7	5
50	150	1	5
150	300	2	5
300	600	3	5

Table 2
SDD count rate and dead-time during a depth scan from 0 to 150 µm at 9 keV.

Position (µm)	Fluorescent count rate	Dead-time (%)
0	6621	9.3
50	6245	8
100	3277	3.4
150	1051	1.5

XANES scanning parameters are shown in Table 1. The SDD count rate during the depth scan from 0 to 150 µm is also given in Table 2.

In confocal fluorescence mode, the fluorescence self-absorption, which distorted the XAS spectra, may be of concern when the target elements in specimens are both thick and concentrated (Lühl *et al.*, 2012). Since the content of copper is less than 0.1% (Lu *et al.*, 2016) and copper contributes 0.5% to the absorption, the fluorescence self-absorption is negligible in our measurement, and the XAS spectra are undistorted. The spectra were processed using the program *ATHENA* (Ravel & Newville, 2005), based on the *IFEFFIT* library (Newville, 2001).

3. Application: depth-resolved structure analysis of sacrificial red glaze (AD 1368–1644) china

XANES is sensitive to the local environment around the absorbing atoms, and thus it can be used to distinguish the

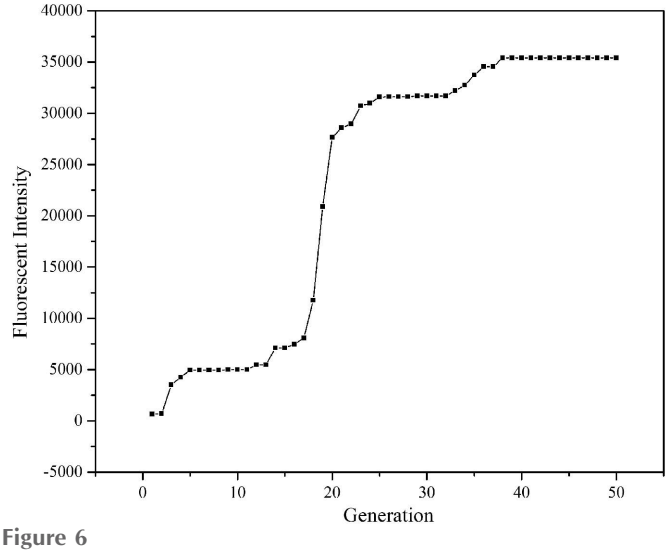

Figure 6
Performance of the adjustment program on the second PHL.

chemical species of copper. Here, depth-resolved XANES is applied to sacrificial red glaze to investigate the depth dependence of the chemical species of copper and its coloration mechanism. XANES profiles for the sacrificial red glaze at various depths are displayed in Fig. 7, using the spectra of copper foil, cuprite (Cu_2O) and tenorite (CuO) as standard references. In metallic form, the absorption *K*-edge of the copper foil is observed at 8979 eV (labeled A), and there are two crests at 8993.4 eV (labeled B) and 9002.3 eV (labeled C). The absorption edge of copper in a higher oxidation state is shifted to a higher photon energy. It can be observed that the edge peak of Cu_2O is shifted to 8981.3 eV, followed by a crest at 8993.9 eV. The intensity of the edge peak will be enhanced when Cu^+ exists in a glass system (Zhu *et al.*, 2014; Klysubun *et al.*, 2011; Farges *et al.*, 2006; Nakai *et al.*, 1999). Compared with the standard, it is shown in Fig. 7 that, deeper in the sample, the valence of copper element is decreased.

Linear combination fitting was performed on these XANES spectra using standards of Cu, CuO, Cu_2O and Cu_2O in glass. The fitting result given in Table 3 indicates that the ratio of Cu^0 to Cu^{1+} increased with increasing sample depth. As reported, Cu^{1+} glass exists in a colorless form, while metallic copper and Cu_2O are the two major elements responsible for the red coloring (Kikugawa *et al.*, 2014). They have two different color mechanisms: one is the surface plasmon effect due to the presence of metallic copper nanoclusters, and the other is the precipitation of reddish Cu_2O crystals in the matrix. The deeper the position in the sample, the higher the ratio of Cu^0 to Cu^{1+}. This depth-related descending valence corresponds to the color evolution from transparent layer to red layer. This result also suggests that metallic copper nanoclusters may be the origin of the red coloring of sacrificial red glaze.

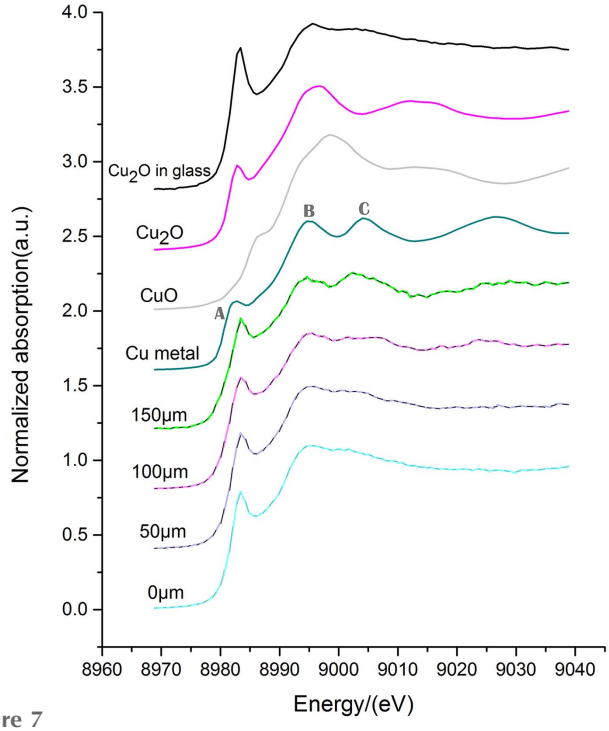

Figure 7
Depth-resolved Cu *K*-edge XANES spectra of the sacrificial red glaze.

Table 3
Best-fitting result of Cu *K*-edge XANES spectra at a depth position from 0 to 150 μm (fitting region: 8969–9029 eV).

Depth position	CuO	Cu_2O	Cu_2O in glass	Cu^{0+}
0 μm	0.151	0.109	0.661	0.079
50 μm	0.091	0.092	0.687	0.131
100 μm	0.000	0.091	0.590	0.319
150 μm	0.000	0.000	0.480	0.520

4. Conclusion and future development

We have constructed a confocal depth-resolved micro-X-ray absorption spectroscope at a general XAS station at Beijing Synchrotron Radiation Facility as a mobile endstation for use on multiple beamlines.

Confocal XAS was applied to sacrificial red glaze to investigate the depth dependence of the chemical species of copper and its coloration mechanism. This can also be used for the non-invasive and depth-resolved structure analysis of fossils and solid/liquid interfaces, extending synchrotron radiation capabilities available to a wider user community.

Funding information

The following funding is acknowledged: National Natural Science Foundation of China (award No. 11375229; award No. 11135008; award No. 11375027; award No. 11275265).

References

Aksenov, V. L., Koval'chuk, M. V., Kuz'min, A. Y., Purans, Y. & Tyutyunnikov, S. I. (2006). *Crystallogr. Rep.* **51**, 908–935.
Choudhury, S., Hormes, J., Agyeman-Budu, D. N., Woll, A. R., George, G. N., Coulthardd, I. & Pickering, I. J. (2015). *J. Anal. At. Spectrom.* **30**, 759–766.
Denecke, M. A., Brendebach, B., De Nolf, W., Falkenberg, G., Janssens, K. & Simon, R. (2009). *At. Spectrosc.* **64**, 791–795.
Farges, F., Etcheverry, M.-P., Scheidegger, A. & Grolimund, D. (2006). *Appl. Geochem.* **21**, 1715–1731.
Gautier-Soyer, M. (1998). *J. Eur. Ceram. Soc.* **18**, 2253–2261.
Guilherme, A., Coroado, J., dos Santos, J. M. F., Lühl, L., Wolff, T., Kanngießer, B. & Carvalho, M. L. (2011). *At. Spectrosc.* **66**, 297–307.
Janssens, K., Proost, K. & Falkenberg, G. (2004). *At. Spectrosc.* **59**, 1637–1645.
Kanngießer, B., Malzer, W., Mantouvalou, I., Sokaras, D. & Karydas, A. G. (2011). *Appl. Phys. A*, **106**, 325–338.
Kanngießer, B., Malzer, W. & Reiche, I. (2003). *Nucl. Instrum. Methods Phys. Res. B*, **211**, 259–264.
Kikugawa, T., Abe, Y., Nakamura, A. & Nakai, I. (2014). *Jpn Soc. Anal. Chem.* **63**, 31–40.
Klysubun, W., Thongkam, Y., Pongkrapan, S., Won-in, K., T-Thienprasert, J. & Dararutana, P. (2011). *Anal. Bioanal. Chem.* **399**, 3033–3040.
Lu, C., Jiang, J. & Xu, C. (2016). *J. Univ. Chin. Acadmey Sci.* **33**, 430–435.
Lühl, L., Hesse, B., Mantouvalou, I., Wilke, M., Mahlkow, S., Aloupi-Siotis, E. & Kanngießer, B. (2014). *Anal. Chem.* **86**, 6924–6930.
Lühl, L., Mantouvalou, I., Malzer, W., Schaumann, I., Vogt, C., Hahn, O. & Kanngießer, B. (2012). *Anal. Chem.* **84**, 1907–1914.
Malzer, W. & Kanngießer, B. (2005). *At. Spectrosc.* **60**, 1334–1341.
Nakai, I., Numako, C., Hosono, H. & Yamasaki, K. (1999). *J. Am. Ceram. Soc.* **82**, 689–695.

Nakano, K., Nishi, C., Otsuki, K., Nishiwaki, Y. & Tsuji, K. (2011). *Anal. Chem.* **83**, 3477–3483.
Nakano, K. & Tsuji, K. (2009). *X-ray Spectrom.* **38**, 446–450.
Newville, M. (2001). *J. Synchrotron Rad.* **8**, 322–324.
Peng, S., Liu, Z., Sun, T., Ma, Y., Sun, W., Zhao, W., He, J., Zhao, G. & Ding, X. (2013). *Nucl. Instrum. Methods Phys. Res. A*, **729**, 565–568.
Ravel, B. & Newville, M. (2005). *J. Synchrotron Rad.* **12**, 537–541.
Rehr, J. J. & Ankudinov, A. L. (2005). *Coord. Chem. Rev.* **249**, 131–140.
Silversmit, G., Vekemans, B., Nikitenko, S., Schmitz, S., Schoonjans, T., Brenkerc, F. E. & Vinczea, L. (2010). *Phys. Chem. Chem. Phys.* **12**, 5653–5659.
Silversmit, G., Vekemans, B., Nikitenko, S., Tirez, K., Bras, W., Brenker, F. E. & Vincze, L. (2009). *J. Phys. Conf. Ser.* **190**, 012036.
Sun, T. & Ding, X. (2015). *Rev. Anal. Chem.* **34**, 45.
Tack, P., Bauters, S., Mauro, J. C., Smedskjaer, M. M., Vekemans, B., Banerjee, D., Bras, W. & Vincze, L. (2016). *RSC Adv.* **6**, 24060–24065.
Wei, X. J., Lei, Y., Sun, T. X., Lin, X. Y., Xu, Q., Chen, D. L., Zou, Y., Jiang, Z., Huang, Y. Y., Yu, X. H., Ding, X. L. & Xu, H. J. (2008). *X-ray Spectrom.* **37**, 595–598.
Xi, S., Borgna, L. S., Zheng, L., Du, Y. & Hu, T. (2017). *J. Synchrotron Rad.* **24**, 367–373.
Zhu, J., Duan, H., Yang, Y., Guan, L., Xu, W., Chen, D., Zhang, J., Wang, L., Huang, Y. & Wang, C. (2014). *J. Synchrotron Rad.* **21**, 751–755.
Zi, M., Wei, X., Yu, H., Lei, Y. & Huang, Y. (2015). *Nucl. Tech.* **38**, 060101.
Zoeger, N., Streli, C., Wobrauschek, P., Jokubonis, C., Pepponi, G., Roschger, P., Hofstaetter, J., Berzlanovich, A., Wegrzynek, D., Chinea-Cano, E., Markowicz, A., Simon, R. & Falkenberg, G. (2008). *X-ray Spectrom.* **37**, 3–11.